# The Donor−Supply Electrode Enhances Performance in Colloidal Quantum Dot Solar Cells

Pouya Maraghechi,[†] André J. Labelle,[†] Ahmad R. Kirmani,[‡] Xinzheng Lan,[†,§] Michael M. Adachi,[†] Susanna M. Thon,[†] Sjoerd Hoogland,[†] Anna Lee,[†] Zhijun Ning,[†] Armin Fischer,[†] Aram Amassian,[‡] and Edward H. Sargent[†,]*

[†]Department of Electrical and Computer Engineering, University of Toronto, Toronto, Ontario M5S 3G4, Canada, [‡]King Abdullah University of Science and Technology (KAUST), Physical Sciences and Engineering Division, Thuwal 23955-6900, Saudi Arabia, and [§]School of Materials Science and Engineering, Hefei University of Technology, 193 Tunxi Road, Hefei, Anhui Province 230009, China

ABSTRACT Colloidal quantum dot (CQD) solar cells combine solution-processability with quantum-size-effect tunability for low-cost harvesting of the sun's broad visible and infrared spectrum. The highest-performing colloidal quantum dot solar cells have, to date, relied on a depleted-heterojunction architecture in which an n-type transparent metal oxide such as TiO_2 induces a depletion region in the p-type CQD solid. These devices have, until now, been limited by a modest depletion region depth produced in the CQD solid owing to limitations in the doping available in TiO_2. Herein we report a new device geometry—one based on a donor−supply electrode (DSE)—that leads to record-performing CQD photovoltaic devices. Only by employing this new charge-extracting approach do we deepen the depletion region in the CQD solid and thereby extract notably more photocarriers, the key element in achieving record photocurrent and device performance. With the use of optoelectronic modeling corroborated by experiment, we develop the guidelines for building a superior CQD solar cell based on the DSE concept. We confirm that using a shallow-work-function terminal electrode is essential to producing improved charge extraction and enhanced performance.
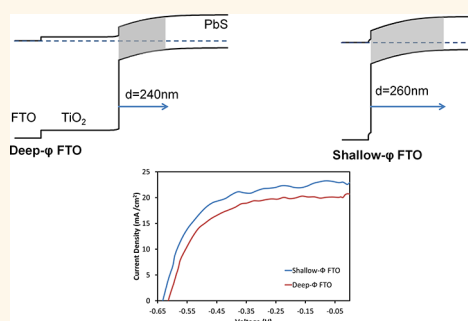
KEYWORDS: donor−supply electrode · colloidal quantum dot · photovoltaics · solar cells · atomic layer deposition · charge-transfer doping

Colloidal quantum dot (CQD) solar cells have attracted attention in light of their ease of fabrication, their potential for low-cost manufacturing, and their roadmap to high efficiency enabled by quantum-size-effect-tuning to harvest the sun's broad visible and infrared spectrum.[1−10] Power conversion efficiencies (PCEs) have improved steadily as device architectures have progressed. Since the first reports of >1% PCE-devices based on the Schottky device architecture,[11−13] certified efficiencies have improved to above 7% PCE through the use of the depleted-heterojunction (DH) architecture, in which a heterojunction is formed by a moderately doped wide-band-gap semiconductor such as TiO_2 and a light-absorbing p-type CQD solid.[1,10]

The power conversion efficiency of CQD solar cells is curtailed today by the fact that short-circuit current densities lie significantly below their theoretical potential. This has been shown to originate from an absorption-extraction compromise, wherein the photon absorption length in the infrared exceeds the transport length. To date, the total transport length, or extraction depth, into the quantum dot film has been dominated by the contribution to photocurrent from photocharge generation occurring within the depletion region.[14]

If significant increases in the depletion region width are to be obtained within the existing depleted heterojunction architecture, they will require large increases in TiO_2 doping levels. Unfortunately, prior studies have indicated that adding various metal dopants to TiO_2 primarily modulates its electron affinity, and not its net free carrier density.

Here we therefore pursue a new experimental strategy. The approach has been proposed from modeling, but not previously

exploited to enhance experimentally measured device performance. The electrode strategy is termed the donor−supply electrode (DSE). It was previously used to overcome the limitations of low-temperature-processed TiO_2 electrodes interfaced with 1 eV quantum dots.[15] In this prior work, a heavily doped n-type layer (aluminum-doped zinc oxide) induced charge injection into a low-doped TiO_2 film and helped overcome the mobility limitations of low-temperature-deposited sputtered TiO_2.[15]

Our goal in the present work is instead to implement the DSE concept in a manner that will increase the overall performance of CQD solar cells beyond previous records. Here we enhance the free carrier density in the n-type electrode *via* charge-injection doping. We use control over the donor layer to induce a deeper depletion region in the CQD film that leads to stronger current extraction. We find that experiment and optoelectronic modeling together support the above picture of the origins of enhanced device performance.

RESULTS AND DISCUSSION

The energy-band diagram of a standard DH CQD solar cell is illustrated in Figure 1a. Light is absorbed in the size-tuned CQD film, and electrons and holes are then separated by the action of the depletion region formed at the n-TiO_2:p-CQD interface, with electrons traveling to the TiO_2 and holes toward a top ohmic contact. Beneath the TiO_2, a 300 nm-thick fluorine-doped tin oxide (FTO) layer acts as the highly conducting transparent electrode. The typical level of doping achieved for TiO_2 is $\sim 5 \times 10^{17}$ cm^{-3}.[15] The light-absorbing PbS layer is $\sim$400 nm thick and has a net free hole density of $\sim 10^{16}$ cm^{-3}. Its optical bandgap is 1.3 eV, and its electron affinity is estimated to be 3.8 eV from cyclic voltammetry measurements.[1] The depletion region inside the PbS layer is calculated (*via* electro-optical simulations (SCAPS))[16] to be $\sim$240 nm in width at zero voltage bias, an estimate consistent with prior capacitance−voltage studies.

We depict in Figure 1b the design requirements for a performance-enhancing DSE. First, the highly doped donor layer (FTO in this work) should have a work function notably shallower than the modestly doped n-type oxide; it is to enhance (TiO_2 herein). Second, for the impact of this highly doped layer to be felt with maximum effect, the TiO_2 layer should be as thin as possible, subject to the requirement that it still form a continuous junction with the PbS.

As seen in Figure 1b, when the work function, Φ, of the FTO is made shallower compared to that of Figure 1a, and the TiO_2 thickness is reduced to 10 nm, electrons from the FTO are injected into the TiO_2 *via* the charge-transfer doping mechanism (Supporting Information, S1). With the thin TiO_2 layer, the charge-transfer doping is more efficient, and a minimum of potential is wasted
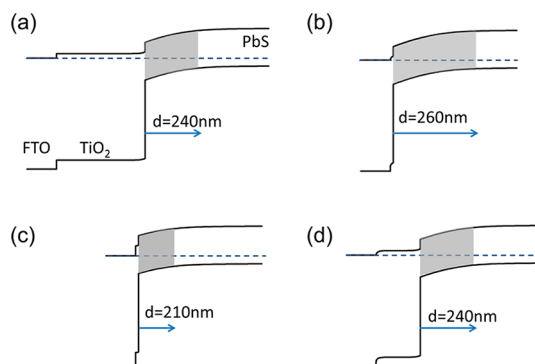

Figure 1. Illustration of the DSE concept using energy-band diagrams of CQD PV devices for (a) a typical PbS CQD PV device with a deep work function FTO layer and a TiO_2 thickness of 300 nm. The width of the depletion region (gray color) inside the PbS film is given by *d*. (b) A shallow work function FTO layer and a thin TiO_2 layer (10 nm). (c) A deep work function FTO layer utilized with 10 nm-thick TiO_2. (d) A shallow work function FTO layer utilized with a 100 nm-thick TiO_2 layer. The combination of shallow work function FTO with a thin TiO_2 layer, as shown in (b), is the optimal DSE implementation and gives the largest depletion region width. The gray areas in the diagrams indicate the extent of the depletion region.

falling across the TiO. Optoelectronic modeling indicates a 10% increase in the depletion width in the PbS film (260 nm) resulting from the increased doping density within the TiO_2. The same modeling predicts a power conversion efficiency (PCE) improvement of 15% from improvements in short-circuit current density (J_{sc}) (reduced recombination from the now-thinner quasi-neutral region), fill-factor (FF) (due to the increased effective doping and thus conductivity of the TiO_2), and open-circuit voltage (V_{oc}) (slightly larger built-in potential), as illustrated in Figure 2.

Motivated by these modeling results, we prepared a suite of CQD solar cells using a similar range of DSE designs. A schematic illustrating the layer structure of our standard devices is shown in Figure 3a.

We used two classes of FTO, one having an appreciably deeper work function than the other (see Supporting Information, S2). Given the uncertainty in extracting absolute quantitative work functions using UPS, we simply label the data for each shallow- and deep-work-function FTO. To control film thicknesses accurately, and additionally to achieve pinhole-free ultrathin layers of TiO_2, we used atomic layer deposition (ALD) to deposit TiO_2 films with different thicknesses on top of the two classes of FTO. The PbS CQD film was deposited *via* a layer-by-layer spin-casting process using 3-mercaptopropionic acid (MPA) for the solid-state exchange. The quantum dots benefited from the hybrid passivation technique, which included exposure to halides in the final stages of their synthesis.[10] The standard thickness of the CQD films was $\sim$380 nm and a MoO_3/Au/Ag stack was evaporated as the top electrode (see Methods). Cross-sectional SEM images of the full devices (with 10 nm TiO_2 films) are
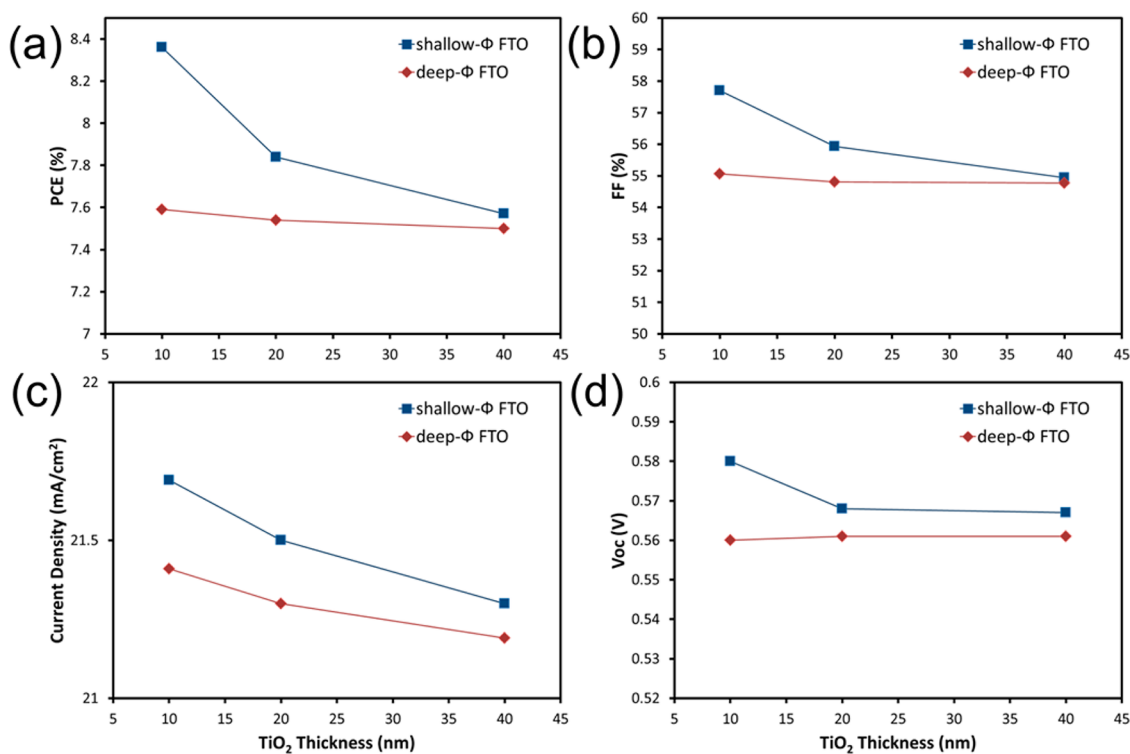
Figure 2. Simulation results for the donor-supply electrode in a CQD PV device. Plots of: (a) PCE, (b) FF, (c) J_{sc}, and (d) V_{oc} as a function of TiO$_2$ thickness for both deep-Φ and shallow-Φ FTO.
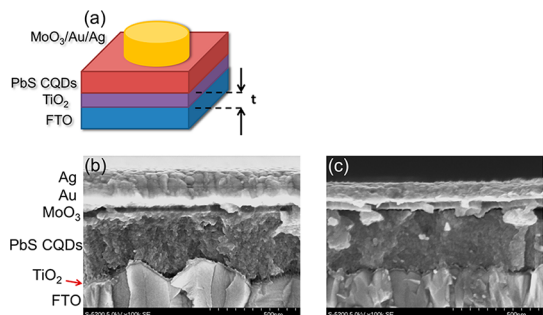

Figure 3. CQD PV device architecture. (a) Schematic of a standard CQD device. The thickness of the TiO$_2$ layer (t) was varied in the devices. The films shown are prepared on a glass substrate. (b) Cross-sectional SEM image of a CQD device on shallow-work function FTO with a 10 nm ALD TiO$_2$ film. (c) Cross-sectional SEM image of a CQD device on deep-work function FTO with a 10 nm TiO$_2$ film.

shown in Figure 3b (shallow-Φ FTO) and Figure 3c (deep-Φ FTO).

Each device was characterized under AM1.5 simulated solar illumination. Figure 4a reports current–voltage plots for these devices. An overall PCE enhancement of 15% was observed for the shallow-Φ FTO devices compared to the deep-Φ FTO devices, with a champion-device efficiency of 8.5%. The enhancement was due to improvements in J_{sc} (22.7 $\pm$ 0.4 vs 20.4 $\pm$ 0.2 mA cm^{-2}), V_{oc} (0.62 $\pm$ 0.01 vs 0.61 $\pm$ 0.01 V) and FF (61 $\pm$ 1% vs 59 $\pm$ 1%). These results are in good agreement with modeling. Uncertainties were calculated by obtaining the standard deviation across eight pixels fabricated on the same substrate and fabrication run.

The device stability was similar to that observed previously for hybrid passivated CQD devices.[10]

Figure 4c shows single-pass absorption spectra for devices fabricated on shallow- and deep-Φ FTO. Light absorption is similar for the two devices, ruling out optical effects related to the different substrates as the major cause of the photocurrent improvement.

External quantum efficiency (EQE) measurements were performed to further investigate the origins of the enhanced photocurrent in the shallow-Φ FTO devices. The EQE results for two representative samples are shown in Figure 4d. The largest fractional enhancement in EQE is in the weakly absorbed NIR range, consistent with a deepened depletion region improving charge extraction farther from the TiO$_2$–CQD interface. Mott–Schottky plots (see Supporting Information, S3) further support the picture of an enhanced depletion region. The effect of TiO$_2$ thickness on device performance for both shallow- and deep-Φ FTO was explored experimentally under AM1.5 simulated illumination (Figure 4b). The experimental results agreed well with the theoretical results presented in Figure 2: the PCE decreases with increased thickness of TiO$_2$ in the shallow-Φ FTO device, consistent with a DSE effect.

To investigate further the dependence of the DSE mechanism on the TiO$_2$ thickness, we prepared and tested devices with 10, 20, and 40 nm thick TiO$_2$ films. In good agreement with modeling results, the experiments demonstrate that the DSE effect is observed only for
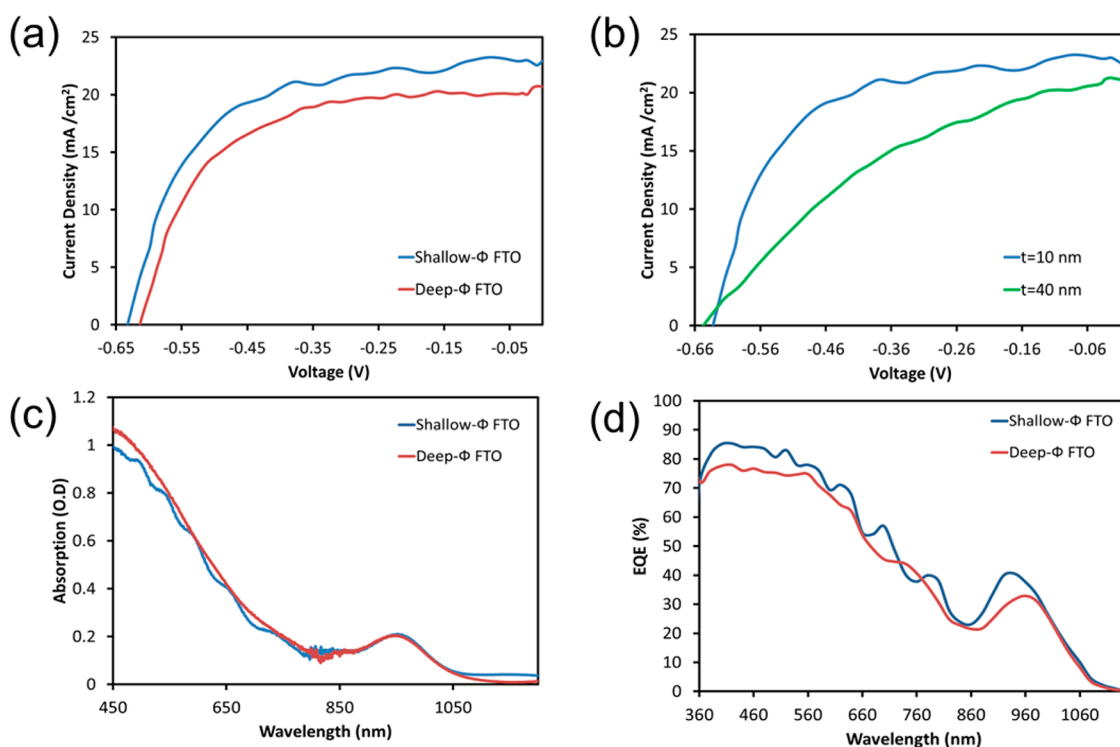
Figure 4. Optical and electrical characterization of CQD PV devices. (a) Light $J-V$ curve for CQD PV devices fabricated on shallow- and deep-Φ FTO with 10 nm thick TiO$_2$ layers. (b) Illuminated $J-V$ curves for CQD PV devices fabricated on shallow-Φ FTO with 10 and 40 nm thick TiO$_2$ layers. (c) Single pass absorption spectra for CQD films on shallow- and deep-Φ FTO devices with 10 nm thick TiO$_2$ layers. (d) External quantum efficiency (EQE) spectra of CQD PV devices fabricated on shallow- and deep-Φ FTO substrates with 10 nm thick TiO$_2$ layers.
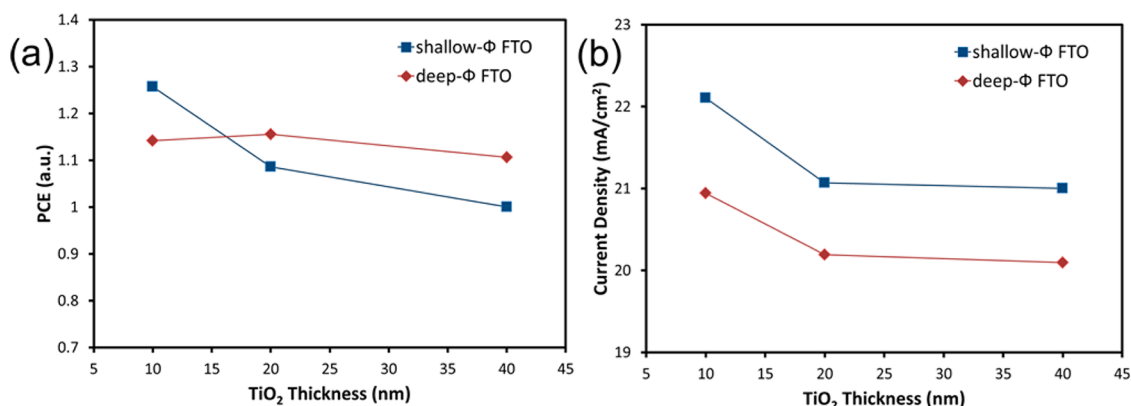

Figure 5. Experimental evidence of a DSE effect. (a) Plot of PCE as a function of TiO$_2$ thickness for both deep- and shallow-Φ FTO devices. (b) Plot of J_{sc} as a function of TiO$_2$ thickness for devices fabricated on shallow-Φ FTO. The values in (a) are normalized to the lowest value of PCE which occurs for the shallow-Φ FTO device with a TiO$_2$ thickness of 40 nm (and are thus presented in arbitrary units).

sufficiently thin TiO$_2$ films (see Figure 5a). For further clarification, the PCE values have been normalized to the lowest value of PCE, which occurs for the shallow-Φ FTO device with a TiO$_2$ thickness of 40 nm.

It is further evident that there is no DSE effect for devices using deep-Φ FTO. For further comparison, J_{sc} is plotted as a function of TiO$_2$ thickness in Figure 5b. These results show that both J_{sc} and PCE are maximized for the 10 nm (thinnest value) thickness of TiO$_2$, demonstrating that a DSE configuration is realized for this thickness.

CONCLUSIONS

In summary, we report a device geometry that leverages a donor–supply electrode to achieve record-performance CQD solar cells. We find that, using this technique, the width of the depletion region in the PbS CQD film is increased by 10%. This is accomplished by employing a shallow-work function transparent electrode coupled with an ultrathin low-doped electron acceptor. Electrons from the highly doped FTO film are injected into TiO$_2$ to achieve charge-transfer doping. The width of the depletion region in the PbS

layer is thereby increased, resulting in increased short-circuit current density and fill factor, ultimately leading to improved power conversion efficiency. Even as the CQD field continues to improve mobility, recombination, and diffusion lengths inside CQD solids, ongoing application of this improved electrode will continue to make the best use of this ever-improving class of materials in optoelectronic device applications.

METHODS

Colloidal Quantum Dot Preparation. The synthesis procedure for the PbS CQDs was based on a previously published recipe.[17] In a three-neck reaction flask, 0.45 g (2.0 mmol) of PbO, 18.0 mL of octadecene (ODE) and 1.5 mL of oleic acid (OA) were pumped at 100 °C under vacuum for ~16 h to dissolve the lead oxide and to degas the solution. In a nitrogen atmosphere glove box, a sulfur precursor solution was prepared by mixing 0.180 mL of bis-(trimethylsilyl)sulfide with 10 mL of ODE. The sulfur solution was quickly injected into the reaction flask at 120 °C, and then the solution was allowed to slowly cool down to room temperature. During the cooling process, when the temperature reached 60 °C, 1.0 mL of metal halide precursor (CdCl$_2$ and tetradecyl-phosphonic acid (TDPA) dissolved in oleylamine with a Cd:TDPA = 13.8:1 molar ratio) was introduced into the reaction flask (as per the hybrid passivation protocol).[10] The PbS CQDs were isolated by the addition of 60 mL of acetone followed by centrifugation after the reaction temperature reached 30−35 °C. The CQDs were then purified by dispersion in toluene and reprecipitation with acetone and redissolved in anhydrous toluene. The solution was washed with methanol three times with the final redispersion in octane at a concentration of 50 mg mL^{-1}.

FTO Material. The shallow-Φ FTO was Asahi Type-U TCO purchased from AGC Solar Company. The deep-Φ FTO was "NSG TEC 15" purchased from Pilkington/NSG Group (see Supporting Information, S4).

CQD Photovoltaic Device Fabrication. The fabrication of CQD films was performed using a layer-by-layer (LBL) spin-casting technique on the FTO substrates. Solid-state ligand exchange was performed in air ambient environment using a 1% 3-mercapto-propionic acid (MPA) solution in methanol. The fabrication process was as follows: (1) 2 drops of PbS CQDs in octane (50 mg mL^{-1}) were dropped onto substrates and were spin-cast at 2500 rpm for 10 s; (2) ~0.2 mL of ligand solution was deposited, followed by spin-drying for 5 s at 2500 rpm; (3) ~0.2 mL of methanol was dropped and spun at 2500 rpm for 10 s (repeated for a total of two times). Steps 1−3 were repeated 10 times to produce the desired PbS CQD film thickness (~380 nm). The top electrode consisted of 10 nm of thermally evaporated molybdenum trioxide deposited at a rate of 0.2 Å s^{-1}, followed by electron-beam deposition of 50 nm of Au deposited at 1.5 Å s^{-1} and capped with 120 nm of thermally evaporated silver deposited at 3.0 Å s^{-1}.

TiO$_2$ Deposition. Atomic layer deposition (ALD) of TiO$_2$ was carried out in a Cambridge NanoTech ALD-Savannah system at 150 °C using Tetrakis(dimethylamido)titanium(IV) (TDMAT) and water (H$_2$O), as the metallic precursor and oxygen source, respectively. The TDMAT precursor was heated to 75 °C. Growth per cycle (GPC) was 0.45 ± 0.01 Å/cycle for the titanium dioxide as measured by spectroscopic ellipsometry. Each ALD cycle included a 100 ms TDMAT precursor dose followed by a 20 s nitrogen gas purge step and a 15 ms H$_2$O precursor dose followed by 20 s of purging. The substrates were further placed in a 120 mmol solution of TiCl$_4$ in deionized (DI) water and heated in an oven for 30 min at 70 °C. Next, the samples were removed from the solution, rinsed with DI water and sintered on a hot plate for 45 min at 520 °C.

AM1.5 Photovoltaic Device Characterization. All photovoltaic device measurements were done under inert N$_2$-flow. Light current−voltage measurements were done using a Keithley 2400 source meter with illumination from a solar simulator (Solar Light, XPS 200, intensity = 100 mW cm^{-2}). A Melles-Griot broadband power meter was used to measure the light source intensity through a circular 0.049 cm^2 aperture. The spectral mismatch of the system was characterized using a calibrated reference solar cell (Newport). The total AM1.5 spectral mismatch—taking into account the simulator spectrum and the spectral responsivities of the test cell, reference cell, and broad-band power meter—was ~5%. This multiplicative factor, M = 0.95, was applied to the current density values of the $J−V$ curve to most closely approximate true AM1.5 performance. The uncertainty of the light current−voltage measurements was 7%, taking into account the temporal fluctuations in the lamp source which falls within the characteristics of class-A specification. The reported values of V_{oc}, J_{sc}, and PCE were averaged over 8 data points during static measurements. During each measurement run, we acquired the static values of J_{sc}, V_{oc} and PCE by holding the cell at short circuit, open circuit, and the bias value corresponding to the maximum power point, respectively, for 20 s to confirm device stability.

Absorption Measurements. A UV−vis-NIR spectrophotometer equipped with an integrating sphere was used for absorption spectra measurements. The absorption measurements were acquired with the sample tilted at a slight angle relative to the illumination beam with all ports other than the illumination port closed. This was to ensure that all directly transmitted, reflected, and off-angle-scattered light was collected by the detector. The 100% transmission baselines for all curves were measured with a bare FTO-coated glass substrate in similar fashion.

External Quantum Efficiency Measurements. All photovoltaic device measurements were done under inert N$_2$-flow. The EQE measurement was performed using monochromatic illumination (400 W xenon lamp through a monochromator with order-sorting filters) which was chopped at 220 kHz. In addition, a constant 1 sun intensity white-light source was simultaneously focused on the PV device to provide a white-light bias. The modulated EQE signal was acquired using a Stanford Research Systems lock-in amplifier at short-circuit conditions. For incident power calibration, Newport 818-UV and Newport 818-IR power meters were used. The uncertainty in the EQE measurements was estimated to be ±8%.

Conflict of Interest: The authors declare no competing financial interest.

REFERENCES AND NOTES

1. Pattantyus-Abraham, A. G.; Kramer, I. J.; Barkhouse, A. R.; Wang, X. H.; Konstantatos, G.; Debnath, R.; Levina, L.; Raabe, I.; Nazeeruddin, M. K.; Gratzel, M.; *et al.* Depleted-Heterojunction Colloidal Quantum Dot Solar Cells. *ACS Nano* **2010**, *4*, 3374–3380.

2. Luther, J. M.; Beard, M. C.; Song, Q.; Law, M.; Ellingson, R. J.; Nozik, A. J. Multiple Exciton Generation in Films of Electronically Coupled PbSe Quantum Dots. *Nano Lett.* **2007**, *7*, 1779–1784.

3. Luther, J. M.; Law, M.; Beard, M. C.; Song, Q.; Reese, M. O.; Ellingson, R. J.; Nozik, A. J. Schottky Solar Cells Based on Colloidal Nanocrystal Films. *Nano Lett.* **2008**, *8*, 3488–3492.

4. Ma, W.; Swisher, S. L.; Ewers, T.; Engel, J.; Ferry, V. E.; Atwater, H. A.; Alivisatos, A. P. Photovoltaic Performance of Ultrasmall PbSe Quantum Dots. *ACS Nano* **2011**, *5*, 8140–8147.

5. Wang, X.; Koleilat, G. I.; Tang, J.; Liu, H.; Kramer, I. J.; Debnath, R.; Brzozowski, L.; Barkhouse, D. A. R.; Levina, L.; Hoogland, S.; *et al.* Tandem Colloidal Quantum Dot Solar Cells Employing a Graded Recombination Layer. *Nat. Photonics* **2011**, *5*, 480–484.

6. Choi, J. J.; Wenger, W. N.; Hoffman, R. S.; Lim, Y.-F.; Luria, J.; Jasieniak, J.; Marohn, J. A.; Hanrath, T. Solution-Processed Nanocrystal Quantum Dot Tandem Solar Cells. *Adv. Mater.* **2011**, *23*, 3144–3148.

7. Barkhouse, D. A. R.; Debnath, R.; Kramer, I. J.; Zhitomirsky, D.; Pattantyus-Abraham, A. G.; Levina, L.; Etgar, L.; Graetzel, M.; Sargent, E. H. Depleted Bulk Heterojunction Colloidal Quantum Dot Photovoltaics. *Adv. Mater.* **2011**, *23*, 3134–3138.

8. Tang, J.; Liu, H.; Zhitomirsky, D.; Hoogland, S.; Wang, X. H.; Furukawa, M.; Levina, L.; Sargent, E. H. Quantum Junction Solar Cells. *Nano Lett.* **2012**, *12*, 4889–4894.

9. Rath, A. K.; Bernechea, M.; Martinez, L.; Pelayo Garcia de Arquer, F.; Osmond, J.; Konstantatos, G. Solution-Processed Inorganic Bulk Nano-Heterojunctions and their Application to Solar Cells. *Nat. Photonics* **2012**, *6*, 529–534.

10. Ip, A. H.; Thon, S. M.; Hoogland, S.; Voznyy, O.; Zhitomirsky, D.; Debnath, R.; Levina, L.; Rollny, L. R.; Carey, G. H.; Fischer, A.; *et al.* Hybrid Passivated Colloidal Quantum Dot Solids. *Nat. Nanotechnol.* **2012**, *7*, 577–582.

11. Klem, E. J. D.; MacNeil, D. D.; Cyr, P. W.; Levina, L.; Sargenta, E. H. Efficient Solution-Processed Infrared Photovoltaic Cells: Planarized All-Inorganic Bulk Heterojunction Devices *via* Inter-Quantum-Dot Bridging During Growth from Solution. *Appl. Phys. Lett.* **2007**, 90.

12. Clifford, J. P.; Johnston, K. W.; Levina, L.; Sargent, E. H. Schottky Barriers to Colloidal Quantum Dot Films. *Appl. Phys. Lett.* **2007**, 91.

13. Johnston, K. W.; Pattantyus-Abraham, A. G.; Clifford, J. P.; Myrskog, S. H.; MacNeil, D. D.; Levina, L.; Sargent, E. H. Schottky-Quantum Dot Photovoltaics for Efficient Infrared Power Conversion. *Appl. Phys. Lett.* **2008**, 92.

14. Johnston, K. W.; Pattantyus-Abraham, A. G.; Clifford, J. P.; Myrskog, S. H.; Hoogland, S.; Shukla, H.; Klem, E. J. D.; Levina, L.; Sargent, E. H. Efficient Schottky-Quantum-Dot Photovoltaics: The Roles of Depletion, Drift, and Diffusion. *Appl. Phys. Lett.* **2008**, 92.

15. Koleilat, G. I.; Wang, X.; Labelle, A. J.; Ip, A. H.; Carey, G. H.; Fischer, A.; Levina, L.; Brzozowski, L.; Sargent, E. H. A Donor-Supply Electrode (DSE) for Colloidal Quantum Dot Photovoltaics. *Nano Lett.* **2011**, *11*, 5173–5178.

16. Burgelman, M.; Nollet, P.; Degrave, S. Modelling Polycrystalline Semiconductor Solar Cells. *Thin Solid Films* **2000**, *361*, 527–532.

17. Hines, M. A.; Scholes, G. D. Colloidal PbS Nanocrystals with Size-Tunable Near-Infrared Emission: Observation of Post-Synthesis Self-Narrowing of the Particle Size Distribution. *Adv. Mater.* **2003**, *15*, 1844–1849.